Journal of Materials Chemistry A

ROYAL SOCIETY OF CHEMISTRY

PAPER

View Article Online
View Journal | View Issue

Check for updates

Cite this: J. Mater. Chem. A, 2024, 12, 21987

Charting the electronic structure for discovering low-cost intermetallic catalysts†

Zhengda He and Bin Ouyang *

Received 5th June 2024
Accepted 13th July 2024

DOI: 10.1039/d4ta03880k

rsc.li/materials-a

Discovering affordable, high-performance, and stable catalysts for the hydrogen evolution reaction (HER) and oxygen reduction reaction (ORR) is essential for the commercialization of clean hydrogen technology. In this study, we utilized a high-throughput screening approach combined with electronic structure descriptors to identify new intermetallic catalysts that minimize noble metal contents while maintaining high performance and stability. We screened 2358 binary and ternary intermetallic compounds constructed from 31 common transition metal elements. From the 462 bulk compositions that are synthetically accessible, we enumerated all possible low-Miller-index surfaces (12 057 surfaces in total) with density functional theory calculations. Seven electronic-structure-based descriptors are then applied to pinpoint aqueously stable surfaces offering performance comparable to that of the renowned Pt (111) and Ir (111) surfaces. This process led to the identification of several previously known noble-metal-containing catalysts, as well as a selection of new intermetallic catalysts.

1 Introduction

Noble metals (*e.g.* Pt and Ir) are renowned for their exceptional catalytic abilities for the hydrogen evolution reaction (HER),[1–3] oxygen reduction reaction (ORR),[3–5] and oxygen evolution reaction (OER).[3,6] Despite their excellent catalytic performance, their high cost and scarcity have spurred extensive research into more affordable catalyst alternatives.[7–9] Intermetallic compounds represent a vast reservoir of potential catalysts that could utilize abundant elements while also being catalytically active.[10–17] Unlike pure metals, intermetallic compounds possess rich coordination environments,[18–20] which could lead to distinct electronic structures compared to the same element in its elemental form.[21] This property opens a diverse chemical space for catalysis. Prior studies have demonstrated that intermetallics can reach the activity of noble-metal-based catalysts while lowering the cost of the catalyst. This can be achieved by not only reducing the noble metal content,[5,22] but also by even avoiding the noble metals entirely, as demonstrated with NiZn[23] and Co-based catalysts.[24] This suggests significant potential for intermetallic catalysts that has yet to be fully explored.

The high throughput screening of catalysts is primarily driven by electronic-structure-based descriptors,[25–28] which are crucial for determining a material's catalytic properties, such as adsorption energy. Commonly used electronic-structure-based descriptors include d-band shape metrics from the Newns–Anderson model,[29–31] which can be represented using the *n*th moment descriptors of the d band, particularly the d-band center (1st moment),[32,33] d-band width (2nd moment),[34] d-band skewness (3rd moment)[34–36] and d-band kurtosis (4th moment)[35–37] as well as the upper band edge.[34] These descriptors, while useful, may not capture all relevant electronic structure information, leading to interest in using the entire density of states (DOS) for a more comprehensive analysis;[38,39] particularly, the DOS has been used as an input feature in the machine learning model for predicting adsorption energies.[39]

In this work, we present a comprehensive screening of 2358 experimental and hypothetic intermetallic compounds hosted in the Materials Project.[40] From this pool, 462 synthetically accessible bulk intermetallic compositions have been identified. Based on the selected bulk phases, 12 057 low-Miller-index surfaces were investigated by performing high-throughput density functional theory (DFT) calculations (the workflow of this work is shown in Fig. 1; details can be seen in the Methods section). Utilizing the aforementioned descriptors, we pinpointed promising intermetallic catalysts, including both previously recognized and newly discovered candidates. Our investigation also includes a detailed analysis of new intermetallic catalysts showing good aqueous stability, with our insights and findings presented at the end of the study.

2 Methods

2.1 Structural models for bulk phases and surfaces

We selected 31 common transition metals from the periodic table, including all 3d, 4d, and 5d metals (except Hg) as well as Ce and Sm. As illustrated in Fig. 1a, using these selected metals,

Department of Chemistry and Biochemistry, Florida State University, Tallahassee, FL, 32304, USA. E-mail: bouyang@fsu.edu

† Electronic supplementary information (ESI) available. See DOI: https://doi.org/10.1039/d4ta03880k

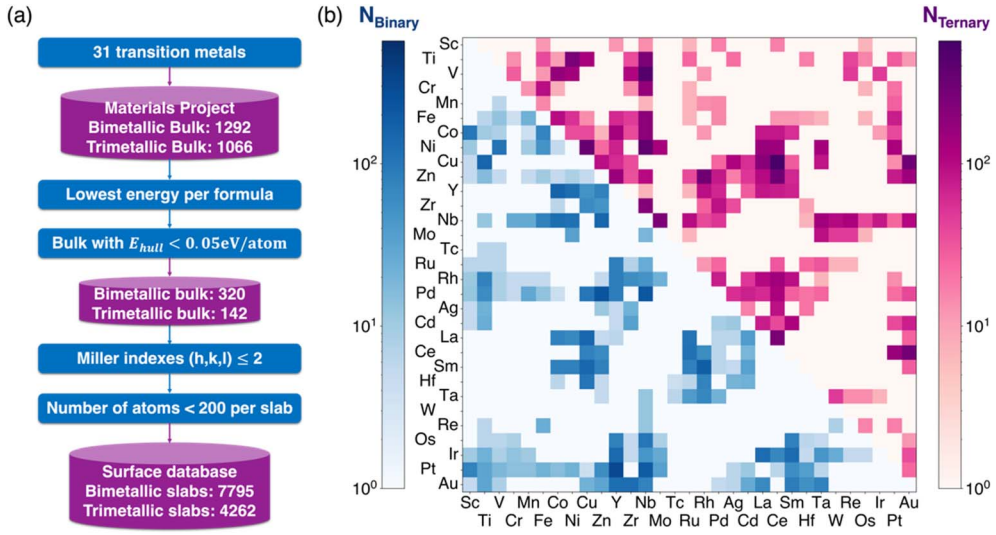

Fig. 1 High-throughput workflow and coverage of chemical space. (a) Schematic figure of the workflow for generating intermetallic surfaces. Blue boxes represent selection criteria and purple areas represent the description of the database. (b) Coverage of chemical space for binary (colored in blue) and ternary (colored in purple) intermetallic surfaces. The color map indicates the number of intermetallic surfaces.

1292 binary and 1066 ternary bulk intermetallic compounds are extracted from the Materials Project.[40] We then selected the structure with the lowest energy for each composition and energy above the hull smaller than 0.05 eV per atom, considering those materials are more likely to be synthetically accessible.[41,42] This selection process narrowed the entries down to 320 binary and 142 ternary intermetallic compounds. For these selected compounds, we generated low-Miller-index surfaces with a maximal Miller index no larger than two.[43] Considering the high computational cost of surface calculations, surfaces that have more than 200 atoms were excluded. Consequently, this process produced a final list of 7795 binary and 4262 ternary surface slabs. In preparing surface models for DFT calculations, we ensured that each periodic dimension was at least 8 Å in length and included a 15 Å vacuum layer to eliminate interactions along the non-periodic direction. The distribution of all generated surface slabs across different elemental spaces is depicted in Fig. 1b, where blue and purple represent the binary and ternary surfaces, respectively. The color contour in Fig. 1b correlates with the number of slabs generated in a specific chemical space, with darker colors indicating more slabs generated. A 3D representation of the number of surfaces for ternary intermetallics is given in Fig. S1 in the ESI.†

2.2 Electronic descriptors for surface sites

We employed seven descriptors to analyze the electronic structures of intermetallic surface sites, categorizing them into DOS-shape descriptors and DOS-similarity descriptors. Based on Newns–Anderson theory,[29–31] we identified four DOS-shape descriptors representing the nth moment of the density of states (DOS), specifically: (1) the d-band center (1st moment);[32,33] (2) d-band width (2nd moment);[34] (3) d-band skewness (3rd moment);[35] (4) d-band kurtosis (4th moment).[35,37] Specifically, d-band width (denoted as d_w, second moment) and d-band kurtosis (denoted as d_k, fourth moment) gauge the level of delocalization in the DOS. d-band skewness (denoted as d_s, third moment) indicates the DOS spectrum's asymmetry. Additionally, we also include the upper edge of the d-band (denoted as d_u), which is described as the highest peak position of Hilbert transformed DOS.[34] The physical intuition of d_u is that the d_u dictates the position of the anti-bonding state, which is sometimes considered a more informative descriptor than the d-band center (d_c).[34] The formulae used to calculate DOS-shaped descriptors are summarized in Section 3 of the ESI.† On the other hand, we devised two DOS-similarity descriptors to assess the resemblance between the total DOS and the valence DOS spectrum. The metric for quantifying the similarity between two DOS spectra involves a function that calculates the difference between the spectra, represented as ρ_1 and ρ_2. The difference, $\Delta\rho$, is expressed as $\Delta\rho = \frac{1}{2N}\sum_{i=0}^{N}\frac{({\rho_1}^i - {\rho_2}^i)^2}{{\rho_1}^i + {\rho_2}^i}$, where N denotes the number of data points in the spectra and ${\rho_1}^i$ and ${\rho_2}^i$ are the i-th data points in the spectra.

2.3 Density functional theory calculations

All simulations were calculated by using the Vienna *Ab Initio* Simulation Package (VASP)[44–47] with the PBE functional[48] and projected-augmented-wave (PAW) pseudopotential for treating the core electrons.[45,49] Spin-polarization is adopted for all simulations. A reciprocal space discretization of 25 k-points per $Å^{-1}$ was used to sample the Brillouin zone. The kinetic cutoff energy is 520 eV. The Methfessel–Paxton scheme is used to smooth the partial occupancies for each orbital.[50] The smearing width is 0.2 eV. The convergence criteria for the self-consistent field (SCF) step is 10^{-4} eV. Geometric optimizations were executed until the force on each atom was less than 0.05 eV $Å^{-1}$. Gaussian broadening with 0.2 eV was used for calculating the DOS spectra. The van der Waals (vdW) dispersion correction is not considered in this work because

it has been shown that minor changes in optimal adsorption energies and overpotentials were observed when the vdW correction was applied.[51]

2.4 Pourbaix diagram and decomposition energy

For evaluating the aqueous stability of bulk materials at certain pH and applied potential, we have constructed the Pourbaix diagram of all promising materials selected using the electronic structure descriptors indicated in Section 2.2. The Pourbaix diagram is constructed using pymatgen[43] and the data are from the Materials project.[40] The decomposition energy (denoted as E_d), presented in our paper, represents the energy released when decomposing into the ground states in the Pourbaix diagram, which can be another solid phase, ions or a mixture of multiple phases.[52–54] In this work we calculated two types of E_d values: (1) the E_d across the full range of pH together with the consideration of potential overpotential during the HER/ORR. Such E_d is used to evaluate promising candidates that could be stable under aqueous conditions; (2) the E_d at specific pH, *e.g.* 1 or 13. Such E_d is used to evaluate the stability of selected catalysts in an alkaline or acidic environment.

3 Results

3.1 Distribution of DOS-shape descriptors

The schematics for all DOS-shape descriptors are illustrated in Fig. 2a. The distributions of five DOS-shape descriptors grouped using the elements of active sites are demonstrated in Fig. 2b. The DOS-shape descriptors for reference active sites of iridium (Ir) and platinum (Pt) are depicted as blue and orange dashed lines, respectively. Starting with the d-band center (denoted as d_c, the first moment of DOS) shown in the top panel of Fig. 2b, a distinct periodic pattern is observable across the 3d/4d/5d metals, which are shown in the figure. Within each period, the d-band center decreases as the number of valence electrons increases. The d_c values for Pt and Ir surface sites on Pt (111) and Ir (111), illustrated by the blue and orange dashed lines, intersect mostly with the distribution of late transition metals. This suggests a higher likelihood for 3d metals, such as Co, Ni, and Cu, and 4d metals, including Ru, Rh, and Pd, to exhibit a closer d_c to reference sites in Pt (111) and Ir (111). Notably also from the d_c plot, the d-band center is mainly influenced by the element of the active site, while variations in the coordination environment within intermetallic compounds have a less significant effect, as indicated by the narrow d_c range for each element. Such an observation also aligns with what has been observed in carbon supported single atom catalysts.[55]

The remaining descriptors, with their schematics shown in Fig. 2a, are used to assess additional DOS-shape characteristics, which have been explained in Method Section 2.2. Overall, these four shape descriptors all exhibit periodic patterns aligned with the element species, though with varying degrees of dispersion. Generally, d_w and d_k first increase and then decrease, while d_s steadily increases with the addition of d electrons, and d_u

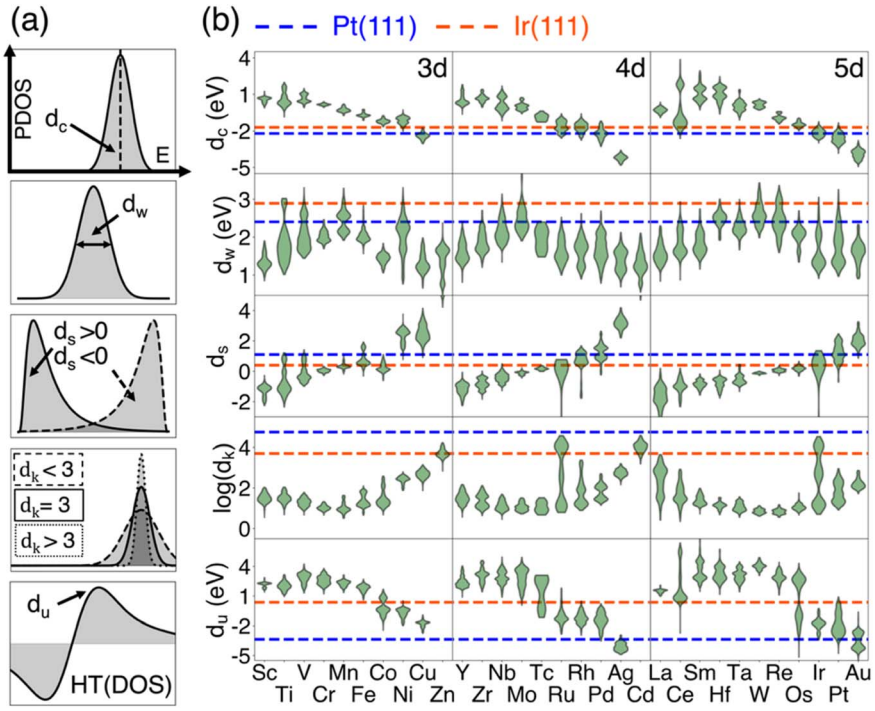

Fig. 2 Distribution of DOS-shape descriptors on all active sites. (a) The schematics of five DOS-shape descriptors have been shown from top to bottom: d-band center (d_c), width (d_w), skewness (d_s), kurtosis (d_k) and upper band edge (d_u); (b) the violin plot for the distribution of the five descriptors. The blue and orange dashed lines represent the values of the descriptors for surface sites at Pt(111) and Ir(111), respectively. For d_c, d_s and d_u, the violins for Zn or Cd are not shown because their location is way beyond the plotted range. The actual positions of Zn and Cd can be found in Fig. S2.† The solid grey lines are the separation between 3d/4d/5d metal elements, and the labels are also shown in each region.

declines as d electrons accumulate. Notably, Pt (111) and Ir (111) references intersect with different elements across these five DOS-shape descriptors, highlighting the potential for predicting catalysts with similar efficacy to Pt or Ir.

3.2 Distribution of DOS-similarity descriptors

In this section, we concentrated on the descriptors related to the similarity of two DOS. As an example, we highlighted two extreme cases of DOS-similarity descriptors that represent the cases of a very similar DOS spectrum ($\Delta\rho = 0.04$) and very different DOS spectrum ($\Delta\rho = 17.8$) in Fig. 3a. The distributions of total-DOS-similarity (denoted as $\Delta\rho_t$) and valence-DOS-similarity (denoted as $\Delta\rho_v$), grouped using the elements of active sites, are shown in Fig. 3b. The trends of both $\Delta\rho_t$ and $\Delta\rho_v$ in a single period (divided by solid grey lines) are all similar regardless of which reference is used. This provides a better generality than the DOS-shape descriptors. We want to choose the surface sites for which the DOS-similarity descriptor has low values, which means that the DOS of the selected surface site is close to that of the reference site. It is clearly observed from Fig. 3b that the late transition metals are, again, the preferred choices, which is consistent with the DOS-shape descriptors such as d_c and d_u. For easy access to all detailed information, we have made an interactive website[56] that includes all surface sites and the values of descriptors for each site.

3.3 Promising catalytic active surfaces with reduced noble metals

With the obtained distribution of all electronic-structure-based descriptors, the top candidates that show the highest similarity on one of the seven descriptors will be selected for further investigation. Further DFT calculations are performed on the top candidates selected to estimate their overpotentials for the HER and ORR. We utilized thermodynamic overpotential (denoted as η) to evaluate the performance of surface sites. Small overpotential represents high activity. The methodology for calculating η of the HER and ORR is shown in Section 2 of the ESI.†

The top candidates, identified using the seven descriptors, will be analyzed with two protocols. In the first protocol, we analyzed all surface sites generated from 462 bulk phases that demonstrate reasonable aqueous stability under HER or ORR conditions. The minimal value of E_d across different pH values (0–14) at certain voltage is used for selecting candidates that are aqueous stable. The cutoffs of E_d ($\min_{pH} E_d^{V=0-0.059pH} < 0.8$ eV per atom for HER catalysts and $\min_{pH} E_d^{V=0.8-0.059pH} < 0.8$ eV per atom) are used to screen the candidates with a low driving force for transforming into other competing phases.[57,58] Such descriptors are built by combining the pre-reported threshold energy for decomposition[53] with the upper bound of overpotential in the HER/ORR. It has been found that materials with decomposition energies smaller than 0.5 eV per atom can be stabilized in an aqueous environment.[53] Since the pool of candidates we focus on is allowed to have overpotential up to 0.3 V above the theoretical overpotential limit, the actual voltage for the HER/ORR will be 0.3 V lower than the theoretical voltage. This adjustment allows for higher decomposition energy at theoretical HER/ORR voltages. We assume that the decomposition energy decreases linearly with the voltage, as the most likely decomposition reaction is $M \rightarrow M^{a+}$ from low voltage to high voltage. Therefore, the final E_d cutoff is set to be 0.8 eV per atom (0.5 eV per atom + 0.3 eV per atom) under theoretical HER/ORR conditions.

Since we did not exclude any elements under the first protocol, our final candidates can contain noble metals. The aqueous stability filter reduces our candidate list from 462 further down to 131 for the HER and 27 for the ORR. The top 10 candidates for the HER and top 10 candidates for the ORR that pass both the descriptor similarity filter and the aqueous stability filter are subjected to further DFT evaluation of overpotentials. The full list of computed overpotentials at promising

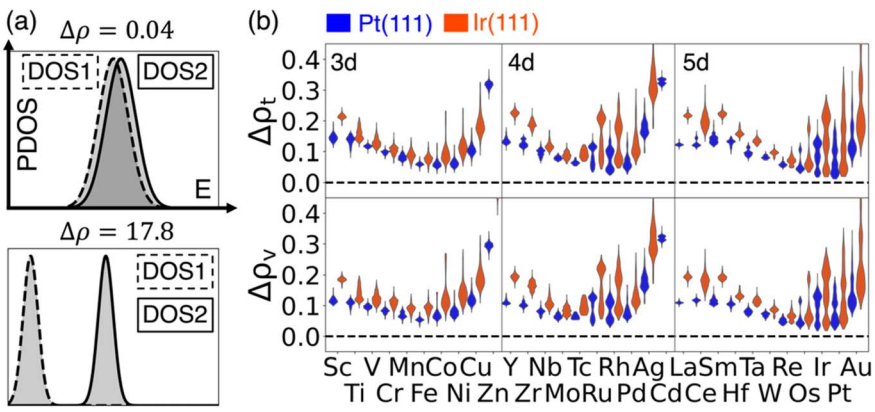

Fig. 3 Distributions of two DOS-similarity descriptors $\Delta\rho$ by using active sites on Pt(111) and Ir(111) as references. (a) The schematics for two DOS spectra that are very similar ($\Delta\rho = 0.04$) and very different ($\Delta\rho = 17.8$). DOS1 (dashed) and DOS2 (solid) represent two selected spectra. The styles of the boxes represent the styles of lines in the figures. (b) Violin plot of the distribution of the total-DOS-similarity descriptor ($\Delta\rho_t$) and valence-DOS-similarity descriptor ($\Delta\rho_v$) using DOS of Pt (111) or Ir (111) as references. The violins for Zn or Cd are partially shown for better visualization because the distribution is out of the selected range (actual position shown in Fig. S3†). The solid grey lines are the separation between 3d/4d/5d metal elements; the labels are also shown in each region.

sites for both the HER ($\eta_{HER} \leq 0.3$ V) and ORR ($\eta_{ORR} \leq 0.8$ V) is shown in Tables S6 and S7,† respectively. The choice of upper bound for HER and ORR overpotentials is based on the minimum overpotentials allowed for the HER (0 V) and ORR (0.37 V)[59] respectively with an extension of 0.3 V for the HER and 0.43 V for the ORR to allow the inclusion of more candidates. All the included candidates that show overpotential within the defined range will hopefully show reasonable performance while accounting for potential errors from DFT simulations.[60]

We showed the top two candidates for the HER (Fig. 4(a and b)) and ORR (Fig. 4(c and d)) that show the lowest overpotential. For each promising active site, we showed three pieces of information: (1) the free energy diagram of the reaction with the computed overpotential on top of each figure; (2) the structure model of the surface with the catalytically active surface site highlighted using a black circle and arrow; (3) the comparison of d-PDOS between the selected surface site and the reference site from Pt (111) or Ir (111). The element of the selected surface site was labeled in bold green text.

For the HER, the Pt site of the Pt_6MnCr (112) surface has the lowest overpotential (with $\eta_{HER} = 0.001$ V), followed by the Ir site in $CrIr_3$ (111) (with $\eta_{HER} = 0.002$ V). In both cases, the active sites are noble metals, but with the incorporation of cheap elements such as Mn/Cr, the total cost of the catalysts can be reduced compared to pure Pt or Ir. These two candidates are generated with the highest similarity of d_c and $\Delta\rho_t$ respectively. For the ORR, the Au site on the Cu_3Au (112) surface has the lowest overpotential ($\eta_{ORR} = 0.4$ V) followed by the Au site on the $CdAu_3$ (100) surface ($\eta_{ORR} = 0.43$ V). These two candidates are selected with the highest similarity of d_w and d_u, respectively.

3.4 Promising catalytic active surfaces without noble metals

Given that the best candidates selected from the first protocol are mostly noble-metal-containing compounds, we developed a second protocol to extend the discovery of noble-metal-free candidates. For the second protocol, we adopt all filters used in the first protocol plus the constraint that the intermetallic surface does not include expensive metals such as Sc, Ru, Rh, Pd, Ag, Re, Os, Ir, Pt, and Au. We also exclude Tc as it is radioactive. Overall, we have 153 noble metal free bulk materials, and after passing the electronic descriptor filter and aqueous stability filter, 27 bulk phases are identified as being stable under HER conditions. The top 3 sites selected using different descriptors are shown in Table S3,† while the top two systems are analyzed in detail and demonstrated in Fig. 5(a) and (b). When it comes to ORR catalyst selection, since we did not find any candidate under our decomposition condition $\min_{pH} E_d^{V=0.8-0.059pH} < 0.8$ eV per atom,

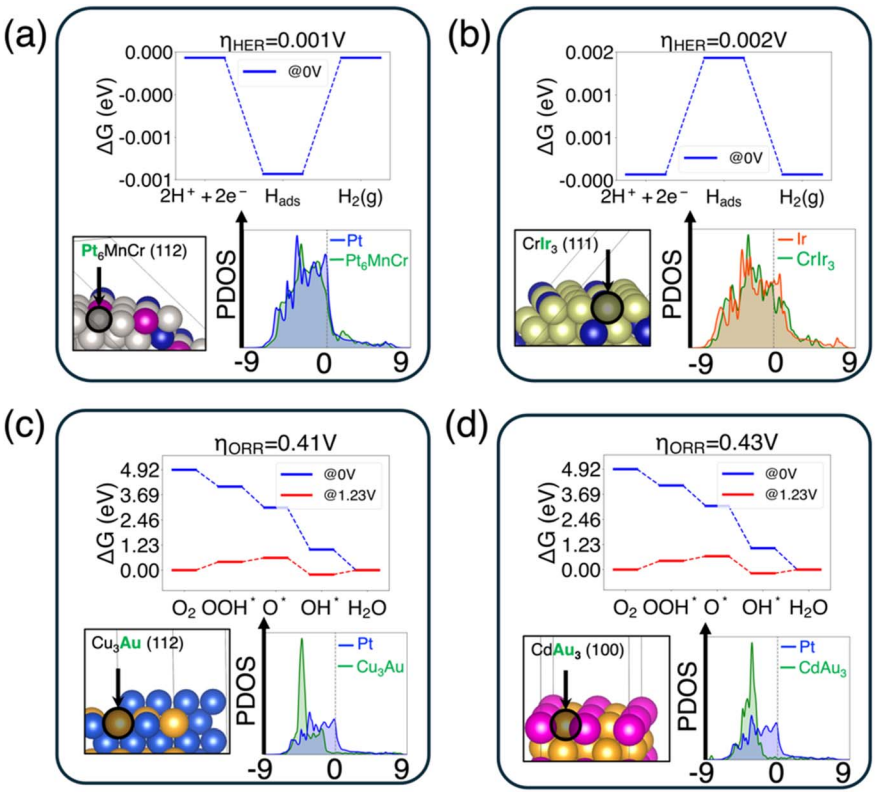

Fig. 4 Best two sites for the HER and ORR selected in the noble-metal-containing pool. The top two candidates for the HER (a and b) and ORR (c and d) on surface sites were selected from the noble-metal-containing pool. For each subfigure, the free energy diagram is shown, along with the structure of the surface with the active site indicated by using an arrow and a shaded circle with a black edge and the comparison between PDOS of the active site and that of the reference surface. For the HER the free energy diagram is only shown at electrode potential equal to 0 V, whereas for the ORR both 0 V and 1.23 V are shown.

we used the same sites selected in the HER and calculated the overpotential of the ORR on each site through DFT.

The results of the top two candidates that show the lowest overpotential for the HER and ORR are shown in Fig. 5, with the same template as in Fig. 4. For the HER, the best surface site is the Co site on the $NbCo_3$ (212) surface (with $\eta_{HER} = 0.022$ V), followed by the Nb site on the $NbNi_3$ (111) surface (with $\eta_{HER} = 0.124$ V). These two candidates are both generated with the best similarity of d_k. When it comes to the ORR, the best surface site is the Cu site on the ZnCu (110) surface (with $\eta_{ORR} = 0.56$ V), followed by the Cu site on the Zn_2CuNi (120) surface (with $\eta_{ORR} = 0.67$ V). These two candidates are both produced by matching d_u.

4 Discussion

4.1 Effectiveness of descriptors

While we've identified several promising new catalysts for both the HER and ORR, it's crucial to recognize that the top candidates selected based on the proposed seven descriptors might not all excel as promising catalysts for the HER and ORR. To assess the effectiveness of these descriptors, we've categorized the distribution of successfully identified new catalysts into four groups. A successful prediction is defined by a candidate demonstrating an overpotential (η) for the HER of ≤0.3 V, or for the ORR of ≤0.8 V, which is also depicted on the *y*-axis of Fig. 6. These catalysts are classified based on whether they contain noble metals or not. The catalysts containing noble metals (denoted as NC) are further segregated into groups for HER catalysts (Fig. 6a) and ORR catalysts (Fig. 6b). Similarly, noble-metal-free (denoted as NF) catalysts are divided into HER (Fig. 6c) and ORR (Fig. 6d) catalysts. By merging all materials derived using Pt (111) and Ir (111) as references, the total count of materials for each category amounts to 40 as shown in Fig. 6a, 20 as shown in Fig. 6b, and 6 as shown in Fig. 6c and d. The computed overpotentials, types of electronic-structure-based descriptors used and aqueous stability at all successfully predicted sites are demonstrated in Tables S6–9.† The correlation between predicted overpotentials and the values of descriptors for both the HER and ORR is summarized in Fig. S5 and S6 in the ESI.†

All seven descriptors generally perform better for predicting noble-metal-containing (NC) intermetallic compounds. The high effectiveness is directly linked to the ease of identifying a noble metal site with similar electronic structures to Pt in Pt (111) or Ir in Ir (111). In contrast, the success rate of all seven descriptors in predicting noble-metal-free (NF) intermetallics is lower. It is notable as shown in Fig. 6c that only half of the best candidates generated by d_w and one third of the best candidates generated by d_k and $\Delta\rho_t$ show reasonable overpotential for the HER, while only d_c and d_u predict reasonable candidates for the ORR (Fig. 6d).

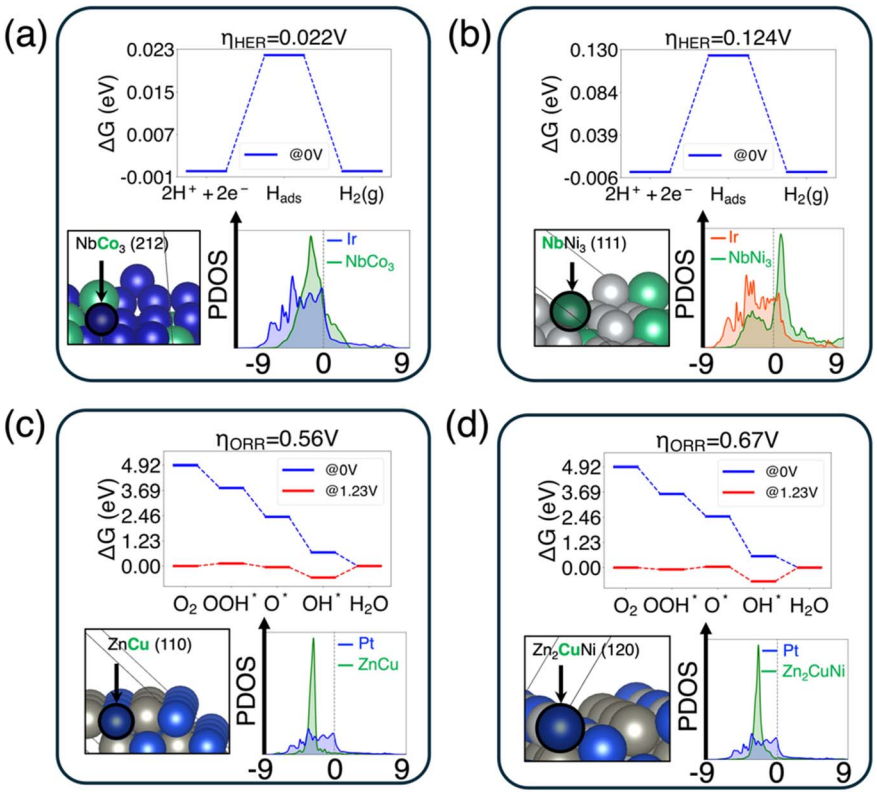

Fig. 5 Best two sites for the HER and ORR selected from the noble-metal-free pool. The top two candidates for the HER (a and b) and ORR (c and d) on sites selected from the noble-metal-free pool. For each subfigure, the free energy diagram is shown, along with the structure of the surface with the active site indicated by using an arrow and a shaded circle with a black edge and the comparison between PDOS of the active site and that of the reference surface. For the HER, the free energy diagram is only shown at electrode potential equal to 0 V, whereas for the ORR both 0 V and 1.23 V are shown.

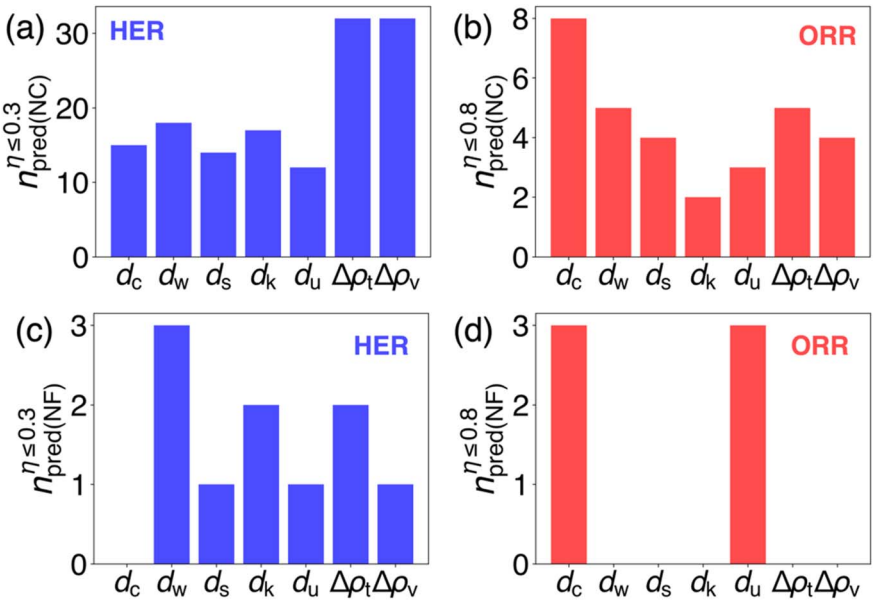

Fig. 6 Effectiveness of descriptors for predicting promising sites for the HER and ORR. The number of predicted promising bulk candidates (denoted as n_{pred}) from using different descriptors for the HER (colored in blue) and ORR (colored in red) based on (a and b) noble-metal-containing (denoted as NC) and (c and d) noble-metal-free (denoted as NF) pools. The selection criteria for overpotentials are indicated in the y-label.

The prediction of good ORR catalysts is generally less successful compared with the prediction of the HER when selecting active sites from both NC and NF pools, particularly when predicting the active site for the ORR from the NF pool (Fig. 6d). In particular, using d_c and d_u, we ended up capturing three good candidates for the ORR per descriptor. The rest of the predictions all fail to generate any promising ORR candidates. This reveals the fact that the ORR process may be more complex than the HER. To name one possibility, the adsorption process of the ORR may be related to the electronic structure of not only the direct adsorption site, but also the sites that are close enough to it. This is mostly because *O, *OH and *OOH groups are much larger compared with the *H group. Many-body interactions are likely to influence the final adsorption energy.

Almost all active sites (181 out of 187) are late transition metal elements. The details of all successful predictions are shown in Tables S6–9 in the ESI.† This phenomenon can be supported as shown in Fig. 2 and 3 as all descriptors will have the best similarity when they have similar numbers of valence electrons. Such behavior reveals more hidden promises of identifying noble-metal-free catalysts among new intermetallic compounds that contain late transition metals.

4.2 Electrochemical stability

Besides catalytic activity, stability under electrochemical conditions is also a crucial criterion for a promising catalyst. The top three candidates in terms of minimizing overpotential are presented in Fig. 7a for HER catalysts and Fig. 7c for ORR catalysts. We also present the top three candidates selected from both NC and NF pools. The Pourbaix diagram for all 12 cases can be found in Fig. S7–10.† Given that noble-metal-free catalysts are more attractive, we present the pourbaix diagrams of the most stable noble-metal-free intermetallic catalysts under aqueous conditions for the HER (Fig. 7b) and for the ORR (Fig. 7d) respectively. The red and blue colors represent acidic and alkaline environments, respectively. It's evident from this figure that the stability of NC candidates supersedes that of NF candidates. This can be attributed to the incorporation of noble metals. It is also observed that the stability of all bulk phases under acidic conditions is lower than those under alkaline conditions, except for $TaNi_6Mo$. This is because when the HER occurs at $TaNi_6Mo$ with reaction potential at -0.24 V (see Table S8†), the decomposition energies of $TaNi_6Mo$ are the same between pH = 1 and pH = 13. A more pronounced trend can be observed when it comes to ORR catalysts, as depicted in Fig. 7c.

Despite the higher stability of intermetallic compounds found under alkaline conditions, the activity of the HER is an order of magnitude lower than that under acidic conditions.[61] In this work, we find some promising candidates for both the HER and ORR that are also stable under acidic conditions (pH = 1). For noble-metal-containing intermetallic compounds, we have Pt_3Zn for the HER (with $\eta_{HER} = 0.002$ V) and Au_3Cu for the ORR (with $\eta_{ORR} = 0.52$ V). For noble-metal-free intermetallic compounds, $TaNi_6Mo$ has the best stability under acidic conditions and good HER performance (with $\eta_{HER} = 0.24$ V). The most stable compound under acidic conditions for the ORR is $ZnCu_2Ni$ (with $\eta_{ORR} = 0.75$ V).

From the Pourbaix diagram shown in Fig. 7b and d, the dissolution of metal sites poses a significant issue for its applications in both the HER and ORR. The dissolution is profound under acidic conditions. In the case of $TaNi_6Mo$, the

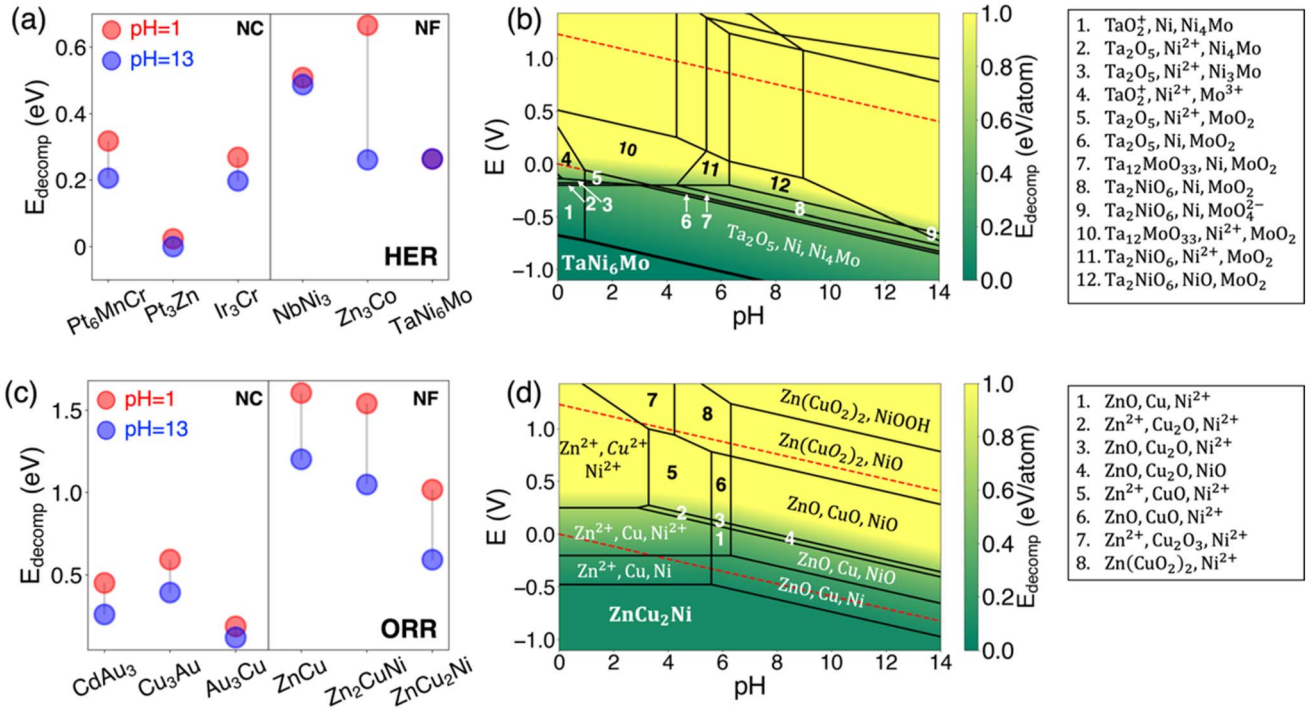

Fig. 7 Aqueous stability of promising intermetallic candidates for the HER and ORR. (a) The decomposition energies (denoted as E_{decomp}) of bulk phases of catalysts for the HER. The top three candidates for NC and NF databases ranked by ascending overpotential are shown. The red and blue represent the values of E_{decomp} at pH = 1 and pH = 13, respectively. (b) Pourbaix diagram of NF catalyst $TaNi_6Mo$, all import regions for the HER are labeled and the corresponding compositions are shown on the right. (c) The E_{decomp} of bulk phases of catalysts for the ORR. The styles are the same as those in (a). (d) Pourbaix diagram of NF catalyst $ZnCu_2Ni$, all import regions for the ORR are labeled and the corresponding compositions are shown on the right.

formation of Ni_4Mo at the standard HER potential, which also serves as an active HER catalyst,[62] could potentially passivate the surface and prevent further dissolution. Under alkaline conditions, the formation of metal oxides is advantageous in preventing further dissolution. In the case of $ZnCu_2Ni$, competitive reactions primarily result in metal oxide formation rather than metal dissolution, which prevents losing metal sites. The oxides formed under alkaline conditions when the ORR happens are also active for the ORR: ZnO,[63] CuO[64,65] and NiO.[66] The slower dissolution rate, coupled with the potential retention of some catalytic activity by the metal oxide, offers a promising pathway for the application of noble-metal-free catalysts for the ORR, especially in alkaline solutions.

4.3 Comparison with the experimental results

Among the bulk phases we have predicted as promising catalysts for the HER and ORR, some of them have already been reported. The Ni–Mo alloy (shown in Table S8,† with $\eta_{HER}^{Ni_3Mo} = 0.29$ V) was reported to show better HER performance than Pt in 1.0 M KOH solution.[62] Nb–Co alloys (shown in Fig. 5a) were shown to have comparable overpotentials of the HER compared with Pt at both 10 mA cm^{-2} and 100mA cm^{-2}.[67] Yang *et al.* also showed that the Nb–Co alloy achieved better HER performance than Pt/C in 1.0 M KOH solution.[68] The Zn–Cu alloy (shown in Fig. 5c) was investigated as an ORR catalyst.[69,70] With such successful predictions of catalysts that have already been verified by experiments, the new candidates predicted, particularly Pt_6MnCr (HER), $CrIr_3$ (HER), $NbNi_3$ (HER) and Zn_2CuNi (ORR) shown in Fig. 4 and 5, as well as $TaNi_6Mo$ (HER), Pd_3Nb (HER), Pt_2FeCo (HER), $CoNi_3$ (HER), and $ZnCu_2Ni$ (ORR) shown in Tables S4, and 5† are likely to deliver promising performance in experiments. We have listed all promising noble-metal-containing (in Table S4†) and noble-metal-free (in Table S5†) catalysts selected from the combination of the activity filter ($\eta_{HER} \leq 0.3$ V and $\eta_{ORR} \leq 0.8$ V) and stability filter ($E_{decomp} \leq 0.5$ eV at reaction potential). We hope that this information can inspire more experimental validations of these predicted catalysts.

5 Conclusion

In this work we have constructed a surface database containing more than 10 000 intermetallic surfaces covering a large area of the chemical space spanned by 31 metal elements. By using seven different electronic-structure-based descriptors, we have successfully identified surface sites that have the potential to reduce cost for the current noble-metal catalysts by either alloying with cheap metal elements or getting rid of the noble metals entirely. Different descriptors have different accuracies in predicting promising surface sites. For the HER, the DOS-similarity descriptors give us the best prediction accuracy. For the ORR, the d-band center and d-band upper edge descriptors

perform the best. We have also investigated the aqueous stability of noble-metal-containing and noble-metal-free intermetallic compounds. Based on our results, not only can noble metal elements be active sites, but they can also increase the aqueous stability of catalysts under reaction conditions. Two promising noble-metal-free catalysts for the HER ($TaNi_6Mo$) and ORR ($ZnCu_2Ni$) were found and their aqueous stabilities were discussed using the corresponding Pourbaix diagrams. We believe that this work will help the development of low-cost, high-performance, and stable catalysts in the future.

Data availability

The values of the proposed seven descriptors on all surface sites can be found in **https://jeff-oakley.github.io/Intermetallic_surface/**. The values of overpotentials at promising sites have been included as part of the ESI.†

Author contributions

Z. H.: *ab initio* simulations, analysis of the data, and writing the original draft. B. O.: conceptualization, *ab initio* simulations, analysis of the data, supervision, and project administration. All authors reviewed and agreed to the final manuscript.

Conflicts of interest

There are no conflicts to declare.

Acknowledgements

We acknowledge support from the startup funding from Florida State University. The computational resources are provided by the Advanced Cyberinfrastructure Coordination Ecosystem: Services & Support (ACCESS), the National Energy Research Scientific Computing Center (NERSC), a DOE Office of Science User Facility supported by the Office of Science and the U.S. Department of Energy under contract no. DE-AC02-05CH11231 and the Research Computing Center (RCC) at Florida State University. The computation and data processing are also supported by the supercomputing resources from the Department of Energy's Office of Energy Efficiency and Renewable Energy at the National Renewable Energy Laboratory.

References

1 C. Li and J.-B. Baek, *ACS Omega*, 2020, **5**, 31–40.
2 J. K. Nørskov, T. Bligaard, A. Logadottir, J. Kitchin, J. G. Chen, S. Pandelov and U. Stimming, *J. Electrochem. Soc.*, 2005, **152**, J23.
3 Z. W. Seh, J. Kibsgaard, C. F. Dickens, I. Chorkendorff, J. K. Nørskov and T. F. Jaramillo, *Science*, 2017, **355**, eaad4998.
4 A. Kulkarni, S. Siahrostami, A. Patel and J. K. Nørskov, *Chem. Rev.*, 2018, **118**, 2302–2312.
5 V. R. Stamenkovic, B. Fowler, B. S. Mun, G. Wang, P. N. Ross, C. A. Lucas and N. M. Marković, *Science*, 2007, **315**, 493–497.
6 Q. Shi, C. Zhu, D. Du and Y. Lin, *Chem. Soc. Rev.*, 2019, **48**, 3181–3192.
7 Y. Nakaya and S. Furukawa, *Chem. Rev.*, 2023, **123**, 5859–5947.
8 V. Vij, S. Sultan, A. M. Harzandi, A. Meena, J. N. Tiwari, W.-G. Lee, T. Yoon and K. S. Kim, *ACS Catal.*, 2017, **7**, 7196–7225.
9 X. Zou and Y. Zhang, *Chem. Soc. Rev.*, 2015, **44**, 5148–5180.
10 S. Furukawa and T. Komatsu, *ACS Catal.*, 2017, **7**, 735–765.
11 E. C. Wegener, B. C. Bukowski, D. Yang, Z. Wu, A. J. Kropf, W. N. Delgass, J. Greeley, G. Zhang and J. T. Miller, *ChemCatChem*, 2020, **12**, 1325–1333.
12 M. Luo, Y. Sun, L. Wang and S. Guo, *Adv. Energy Mater.*, 2017, **7**, 1602073.
13 M. Armbrüster, *Sci. Technol. Adv. Mater.*, 2020, **21**, 303–322.
14 M. Krajčí and J. Hafner, *ChemCatChem*, 2016, **8**, 34–48.
15 J. Hafner and M. Krajčí, *Acc. Chem. Res.*, 2014, **47**, 3378–3384.
16 M. Armbrüster, R. Schlögl and Y. Grin, *Sci. Technol. Adv. Mater.*, 2014, **15**, 034803.
17 L. Rößner and M. Armbrüster, *ACS Catal.*, 2019, **9**, 2018–2062.
18 T. G. Akhmetshina, V. A. Blatov, D. M. Proserpio and A. P. Shevchenko, *Acc. Chem. Res.*, 2018, **51**, 21–30.
19 R. Nesper, *Angew Chem. Int. Ed. Engl.*, 1991, **30**, 789–817.
20 O. A. Blatova, V. T. Osipov, V. E. Pavlova, M. A. Solodovnikova, I. I. Trofimychev, E. M. Egorova and V. A. Blatov, *Inorg. Chem.*, 2023, **62**, 6214–6223.
21 A. S. Rosen, S. Vijay and K. A. Persson, *Chem. Sci.*, 2023, **14**, 1503–1511.
22 Z. Wang, X. Yao, Y. Kang, L. Miao, D. Xia and L. Gan, *Adv. Funct. Mater.*, 2019, **29**, 1902987.
23 Q. Zhou, Q. Hao, Y. Li, J. Yu, C. Xu, H. Liu and S. Yan, *Nano Energy*, 2021, **89**, 106402.
24 P. Zhang, H.-G. Xue and N.-T. Suen, *Chem. Commun.*, 2019, **55**, 14406–14409.
25 S. Jiao, X. Fu and H. Huang, *Adv. Funct. Mater.*, 2022, **32**, 2107651.
26 A. Vojvodic and J. K. Nørskov, *Natl. Sci. Rev.*, 2015, **2**, 140–143.
27 N. Marzari, A. Ferretti and C. Wolverton, *Nat. Mater.*, 2021, **20**, 736–749.
28 B. W. J. Chen, L. Xu and M. Mavrikakis, *Chem. Rev.*, 2021, **121**, 1007–1048.
29 P. W. Anderson, *Phy. Rev.*, 1961, **124**, 41–53.
30 D. M. Newns, *Phy. Rev.*, 1969, **178**, 1123–1135.
31 J. P. Muscat and D. M. Newns, *Prog. Surf. Sci.*, 1978, **9**, 1–43.
32 B. Hammer and J. K. Norskov, *Nature*, 1995, **376**, 238–240.
33 B. Hammer and J. K. Nørskov, *Surf. Sci.*, 1995, **343**, 211–220.
34 H. Xin, A. Vojvodic, J. Voss, J. K. Nørskov and F. Abild-Pedersen, *Phys. Rev. B: Condens. Matter Mater. Phys.*, 2014, **89**, 115114.
35 M. Andersen, S. V. Levchenko, M. Scheffler and K. Reuter, *ACS Catal.*, 2019, **9**, 2752–2759.
36 P. Pankajakshan, S. Sanyal, O. E. de Noord, I. Bhattacharya, A. Bhattacharyya and U. Waghmare, *Chem. Mater.*, 2017, **29**, 4190–4201.
37 L. T. DeCarlo, *Psychol. Methods*, 1997, **2**, 292–307.

38 C. Ben Mahmoud, A. Anelli, G. Csányi and M. Ceriotti, *Phys. Rev. B: Condens. Matter Mater. Phys.*, 2020, **102**, 235130.
39 V. Fung, G. Hu, P. Ganesh and B. G. Sumpter, *Nat. Commun.*, 2021, **12**, 88.
40 A. Jain, S. P. Ong, G. Hautier, W. Chen, W. D. Richards, S. Dacek, S. Cholia, D. Gunter, D. Skinner, G. Ceder and K. A. Persson, *APL Mater.*, 2013, **1**, 011002.
41 W. Sun, S. T. Dacek, S. P. Ong, G. Hautier, A. Jain, W. D. Richards, A. C. Gamst, K. A. Persson and G. Ceder, *Sci. Adv.*, 2016, **2**, e1600225.
42 B. Ouyang, J. Wang, T. He, C. J. Bartel, H. Huo, Y. Wang, V. Lacivita, H. Kim and G. Ceder, *Nat. Commun.*, 2021, **12**, 5752.
43 S. P. Ong, W. D. Richards, A. Jain, G. Hautier, M. Kocher, S. Cholia, D. Gunter, V. L. Chevrier, K. A. Persson and G. Ceder, *Comput. Mater. Sci.*, 2013, **68**, 314–319.
44 G. Kresse and J. Hafner, *Phys. Rev. B: Condens. Matter Mater. Phys.*, 1993, **47**, 558.
45 P. E. Blöchl, *Phys. Rev. B: Condens. Matter Mater. Phys.*, 1994, **50**, 17953.
46 G. Kresse and J. Hafner, *Phys. Rev. B: Condens. Matter Mater. Phys.*, 1994, **49**, 14251.
47 G. Kresse and J. Furthmüller, *Comput. Mater. Sci.*, 1996, **6**, 15–50.
48 J. P. Perdew, K. Burke and M. Ernzerhof, *Phys. Rev. Lett.*, 1996, **77**, 3865.
49 G. Kresse and D. Joubert, *Phys. Rev. B: Condens. Matter Mater. Phys.*, 1999, **59**, 1758.
50 M. Methfessel and A. T. Paxton, *Phys. Rev. B: Condens. Matter Mater. Phys.*, 1989, **40**, 3616–3621.
51 R. Christensen, H. A. Hansen, C. F. Dickens, J. K. Nørskov and T. Vegge, *J. Phys. Chem. C*, 2016, **120**, 24910–24916.
52 K. A. Persson, B. Waldwick, P. Lazic and G. Ceder, *Phys. Rev. B: Condens. Matter Mater. Phys.*, 2012, **85**, 235438.
53 A. K. Singh, L. Zhou, A. Shinde, S. K. Suram, J. H. Montoya, D. Winston, J. M. Gregoire and K. A. Persson, *Chem. Mater.*, 2017, **29**, 10159–10167.
54 A. M. Patel, J. K. Nørskov, K. A. Persson and J. H. Montoya, *Phys. Chem. Chem. Phys.*, 2019, **21**, 25323–25327.
55 Z. He, J. Wang and B. Ouyang, *Chem. Mater.*, 2024, **36**, 1405–1412.
56 **https://jeff-oakley.github.io/Intermetallic_surface/htmls/IntermallicHeatmap.html**, accessed Apr. 2nd, 2024.
57 R. Tran, L. Huang, Y. Zi, S. Wang, B. M. Comer, X. Wu, S. J. Raaijman, N. K. Sinha, S. Sadasivan and S. Thundiyil, *arXiv*, 2023, preprint, arXiv:2311.00784, DOI: **10.48550/arXiv.2311.00784**.
58 A. Jain, Z. Wang and J. K. Nørskov, *ACS Energy Lett.*, 2019, **4**, 1410–1411.
59 M. T. M. Koper, *Chem. Sci.*, 2013, **4**, 2710–2723.
60 S. Deshpande, J. R. Kitchin and V. Viswanathan, *ACS Catal.*, 2016, **6**, 5251–5259.
61 H. Lv, D. Li, D. Strmcnik, A. P. Paulikas, N. M. Markovic and V. R. Stamenkovic, *Nano Energy*, 2016, **29**, 149–165.
62 F. Qin, Z. Zhao, M. K. Alam, Y. Ni, F. Robles-Hernandez, L. Yu, S. Chen, Z. Ren, Z. Wang and J. Bao, *ACS Energy Lett.*, 2018, **3**, 546–554.
63 M. R. Shakil, A. M. El-Sawy, H. Tasnim, A. G. Meguerdichian, J. Jin, J. P. Dubrosky and S. L. Suib, *Inorg. Chem.*, 2018, **57**, 9977–9987.
64 D. Mahato, T. Gurusamy, S. K. Jain, K. Ramanujam, P. Haridoss and T. Thomas, *Mater. Today Chem.*, 2022, **26**, 101167.
65 H. Xiao, B. Li, M. Zhao, Y. Li, T. Hu, J. Jia and H. Wu, *Chem. Commun.*, 2021, **57**, 4118–4121.
66 N. Sandhiran, S. Ganapathy, Y. Manoharan, D. Ganguly, M. Kumar, K. Ramanujam and S. Balachandran, *Environ. Res.*, 2022, **211**, 112992.
67 Z. Gao, S. Yun, C. Yang, Y. Zhang, J. Dang, G. Yang, T. Yang, D. Qiao and K. Wang, *J. Colloid Interface Sci.*, 2023, **639**, 33–48.
68 Y.-Q. Yang, S.-J. Ji and N.-T. Suen, *Inorg. Chem.*, 2023, **62**, 2188–2196.
69 R. Procaccini, S. Ceré and M. Vázquez, *J. Appl. Electrochem.*, 2009, **39**, 177–184.
70 Q. Wang, S. Shi, F. Wu, Z. Zhang, G. Li, Y. Zheng and Y. Suo, *Catal. Lett.*, 2022, **152**, 1950–1960.